Applied Acoustics 224 (2024) 110130

Contents lists available at ScienceDirect

Applied Acoustics

journal homepage: www.elsevier.com/locate/apacoust

A small-scale active anechoic chamber

R. Haasjes [a,*], A.P. Berkhoff [a,b]

[a] University of Twente, Faculty of Engineering Technology, Applied Mechanics and Data Analysis, Drienerlolaan 5, Enschede, 7522 NG, the Netherlands
[b] TNO Acoustics and Sonar, Oude Waalsdorperweg 63, The Hague, 2597 AK, the Netherlands

ARTICLE INFO

Keywords:
Kirchhoff-Helmholtz integral
Preconditioned conjugate gradient
Active noise control
Acoustic anechoic chamber

ABSTRACT

This paper presents a solution method to suppress reflections from the walls in an anechoic room using active control, in which the control coefficients are obtained with an efficient algorithm. One of the main challenges in suppressing the reflections, is the estimation of the reflected sound field, which is a non-measurable quantity. The reflected sound field is computed using the Kirchhoff-Helmholtz integral with a set of microphones on a circle. The effectiveness of the method is shown on an experimental setup. The experimental setup is a small-scale version of an acoustic anechoic chamber. An anechoic chamber, with larger dimensions and higher frequencies, will result in a system with a relatively large number of sources and sensors. It is computationally expensive to find a set of control filters for larger-scale systems. The conjugate gradient algorithm using block-circulant preconditioning is an efficient method to solve for the optimal set of control filters. The preconditioned conjugate gradient algorithm is used together with the Kirchhoff-Helmholtz integral. Real-time measurements show that the reflections are effectively suppressed, expressed in terms of the reverberation time. This results in a small-scale active anechoic chamber.

1. Introduction

Acoustic anechoic chambers are designed to absorb acoustic waves at its boundaries, effectively creating a free space environment that mimics an environment with boundless dimensions. These chambers see frequent use in tasks such as transfer function measurements, sensor calibration, certification of machinery and more [1–3].

Ideally, all the acoustic waves are absorbed at the walls, which allows for a reflection-free environment. However, the thickness of conventional absorption materials cannot be increased enough for technical and economical reasons. Therefore, low-frequency reflections remain [4,5], in some cases even above the cut-off frequency the chamber is designed for. Design principles of an acoustic anechoic chamber are described in [6–8], which highlight the design efforts required to lower the cut-off frequency using conventional passive absorption methods.

Active noise control is effective at lower frequencies, which makes this a promising technique to complement the passive sound absorption. The combination of both passive- and active-techniques seems promising to extend the operable frequency range of an acoustic anechoic chamber. A detailed overview of research directions in active noise control is presented in [9].

The use of measured transfer functions in the design of a controller enables the design of a system with ordinary sources and sensors, thus reducing the cost. It is assumed that the reference signals are stationary in time and that all involved systems are linear time invariant (LTI). The set of optimal filter coefficients, often called the Wiener filter, is found by solving a set of linear equations in the time-domain [10].

For larger geometries and increasing frequencies, the number of sources and sensors increases rapidly. The current performance of active control system is limited by the number of channels that is manageable by today's standards [11,12]. An increase in channels results in an increase in computational complexity. Therefore, previous work has been dedicated to engineering more efficient algorithms to allow for solving larger-scale systems. In the Wiener filtering problem, the system of equations to be solved contains a Toeplitz-block matrix. Efficient algorithms exploit knowledge about the matrix structure to reduce the computational complexity. The Levinson algorithm [13] is well-known, which solves the Wiener filter with $\mathcal{O}(n^2)$ complexity, where n is the size of the Toeplitz-block matrix. Solving the Wiener filtering problem in an iterative manner with the preconditioned conjugate gradient method (PCG) is shown using circulant preconditioning for Toeplitz-block matrices [14]. Other preconditioners have been introduced as well [15,16].

* Corresponding author.
E-mail address: r.haasjes@utwente.nl (R. Haasjes).

https://doi.org/10.1016/j.apacoust.2024.110130
Received 27 March 2024; Received in revised form 22 May 2024; Accepted 13 June 2024
Available online 20 June 2024

A physical approach to expand a finite-size laboratory with a virtual domain using active boundary control, utilizing immersive boundary conditions is shown by [17]. However, this method relies on ideal sources, requiring calibration for which a method is not shown. The immersive boundary conditions have been extended to cloaking and holography [18] and elastic immersive wave experimentations [19,20]. One of the main challenges of the active suppression of reflections, is to get a reliable estimate of the scattered field, which is a non-measurable quantity. Active control in an anechoic room is shown in [21], active control of scattered acoustic radiation in [11] and real-time active suppression of scattered acoustic radiation in [12]. The methods in [11,12,21] apply scattering filters to estimate the reflected sound field. In the case of a scattering object, the scattering filters are estimated by measuring with and without the object. However, in the case of an anechoic chamber, the scattering objects being the boundaries of the chamber, cannot be removed.

A simulation of active control to attenuate acoustic reflections in an anechoic chamber has been shown in [22], which applies the Kirchhoff-Helmholtz integral to compute the reflected sound field. The signals computed with the Kirchhoff-Helmholtz integral (KHI) are minimized by the control algorithm. However, the effectiveness of the method is shown with a simulation, without verification on a real-world application. The efficient algorithm that is presented in [22] applies preconditioning filters in the secondary path to improve convergence. These preconditioning filters introduce delays, so that more time-advance of the reference signals is required. The required time-advance is not available in the small-scale chamber in this paper, due to its smaller dimensions. The PCG algorithm does not have additional filters in the secondary path that introduce delay, which lessens the required time-advancement on the reference signals.

The contribution of this paper is twofold. First, the KHI method is applied on an experimental setup, with the same configuration as used in the simulation shown in [22]. Secondly, this paper shows the practical implementation of a modified PCG algorithm, which incorporates diagonal regularization. The regularization is necessary to maintain a stable system in combination with internal model control (IMC). Although in this paper the control filter coefficients are computed using the PCG algorithm, any other algorithm can be applied with this method, as long as the resulting control coefficients are causal and regularization is applied in combination with IMC. The effectiveness of suppressing the acoustic reflections is evaluated in terms of the reverberation time (RT) measured at the verification sensors. The experimental setup is considered 2-dimensional (2D) within the frequency range of interest. However, the method is also applicable on 3-dimensional (3D) applications by use of a different free-field Greens function in combination with a spherical sensor configuration.

2. Computation of the reflected sound field using the Kirchhoff-Helmholtz integral

The KHI is computed to obtain the reflected sound field. The full derivation, starting from the acoustic wave equation and the Green's integral theorem can be found in [22]. The governing 2D equation is written as:

$$p^{(2)}(\mathbf{x},\omega) = \frac{-\mathrm{j}k}{4}\int_S (j\rho c V_n(\mathbf{x}_s,\omega) H_0^{(2)}(k|\mathbf{x}-\mathbf{x}_s|) + p(\mathbf{x}_s,\omega) H_1^{(2)}(k|\mathbf{x}-\mathbf{x}_s|)\frac{\mathbf{x}-\mathbf{x}_s}{|\mathbf{x}-\mathbf{x}_s|}\cdot\mathbf{n})\,dS, \quad (1)$$

in which S denotes the contour of integration, $\mathrm{j}=\sqrt{-1}$, ρ is the density of the acoustic medium, c is the speed of sound, $V_n(\mathbf{x}_s,\omega)$ is the particle velocity on the surface in the normal inward direction, $H_a^{(b)}$ denotes the Hankel function of kind b and order a and $\mathbf{n}$ is the unit normal inward vector on the surface. In this equation, the 2D free-field Greens function is substituted, written as

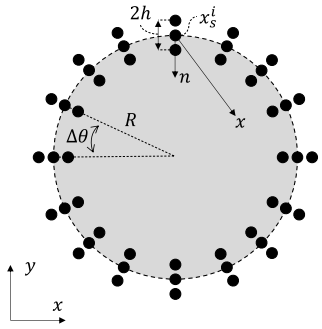

Fig. 1. Geometry used for the discretization of the Kirchhoff-Helmholtz integral in case of a circular microphone array [22].

$$G(\mathbf{x}|\mathbf{x}_s,\omega) = -\mathrm{j}\pi H_0^{(2)}(k|\mathbf{x}-\mathbf{x}_s|). \quad (2)$$

Using a simple geometry, in this case a circle, following the notation of Fig. 1, the equation is discretized and written as [22,23]:

$$p^{(2)}(\mathbf{x},\omega) = \frac{-\mathrm{j}k}{4}\sum_{i=1}^{N_L}(j\rho c V_n(\mathbf{x}_s^i,\omega) H_0^{(2)}(k|\mathbf{x}-\mathbf{x}_s^i|) + p(\mathbf{x}_s^i,\omega) H_1^{(2)}(k|\mathbf{x}-\mathbf{x}_s^i|)\frac{\mathbf{x}-\mathbf{x}_s}{|\mathbf{x}-\mathbf{x}_s|}\cdot\mathbf{n})R\Delta\theta, \quad (3)$$

in which $\Delta\theta$ is the angle between the sensors on the surface, assuming the sensors are equidistantly distributed. The particle velocity in the radial inward direction is obtained following:

$$V_n(\mathbf{x}_s^i,\omega) = \frac{p(r_{s+h}^i,\omega) - p(r_{s-h}^i,\omega)}{2jh\omega\rho}, \quad (4)$$

in which h is the distance between the sensors in radial direction, $r_{s-h}^i = ||\mathbf{x}_s^i|| - h$ and $r_{s+h}^i = ||\mathbf{x}_s^i|| + h$ (in polar coordinates). The sensors on the circle are named the error sensors. With the normal vector $\mathbf{n}$ pointing inward from the contour, as shown in Fig. 1, the output of the KHI is only valid at locations within the contour.

The benefit of this method is that the KHI is easily transformed into its 3D equivalent, by changing the free-field Greens function (Eq. (2)) from the 2D to the 3D equation and by changing the line integral to a surface integral.

If a source is located within the contour, the output of the KHI within the contour is just the reflected sound field. Therefore, this method allows to model the primary path by computing the transfer function from the primary sources to all the error sensors on the circle, followed by the evaluation of the KHI, to obtain the reflected sound field due to the primary sources, named the primary source signal.

If a source is located outside of the contour, the output of the KHI is the sound field. Therefore, the secondary path is modeled by computing the transfer function from the secondary sources to all the error sensors on the circle, followed by the evaluation of the KHI to obtain the sound field due to the secondary sources, named the secondary signals.

The outputs of the KHI are named the performance signals, measured with the virtual performance sensors. The performance sensors are located within the contour at user defined locations. The obtained performance signals are used in the feedforward control scheme and are minimized by the control algorithm. Therefore, this approach directly minimizes the output of the KHI, which means that the sound field reflected from the walls due to the primary sources, summed with the sound field due to the secondary sources, is minimized at the performance sensor locations within the contour.

3. Method

A block diagram of a feedforward active noise control system is shown in Fig. 2. In this scheme, the primary noise signal is the output of the KHI with the primary sources active, which is denoted by

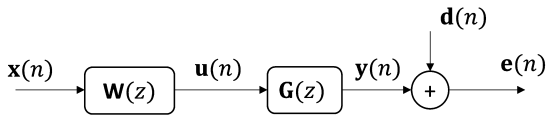

Fig. 2. Block-scheme of a feedforward active noise control system [10].

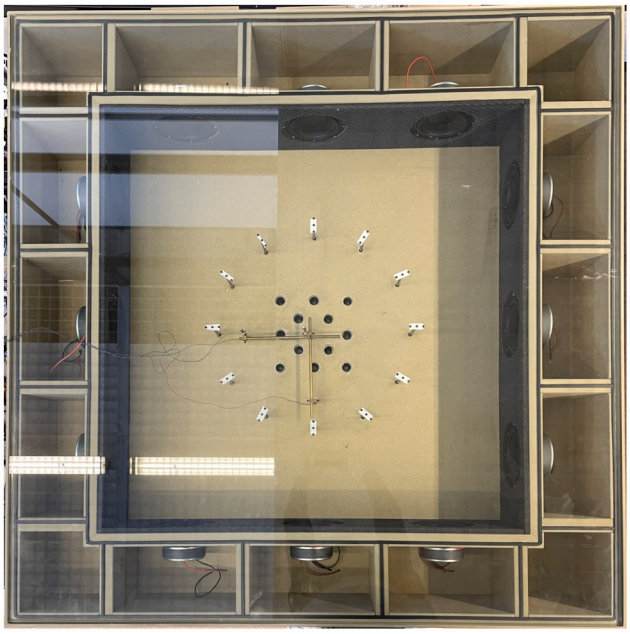

Fig. 3. Top view showing the sensor configuration and the secondary sources of the experimental setup.

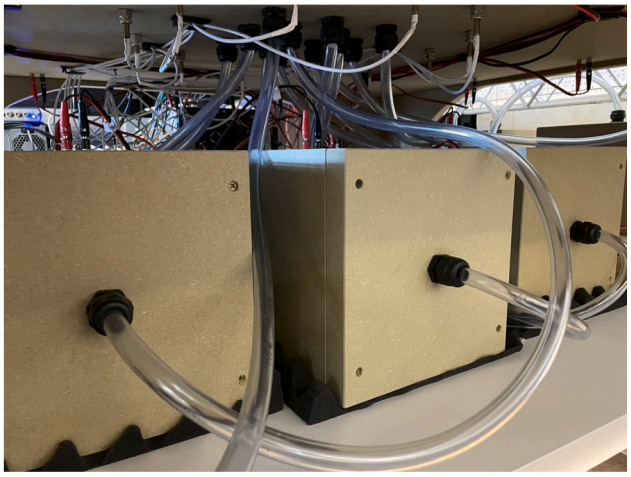

Fig. 4. The external primary sources connected to the bottom of the experimental setup using tubes.

$\mathbf{d}(n) \in \mathcal{R}^{L_{\text{perf}} \times P}$, in which L_{perf} denotes the number of performance sensors, P denotes the number of primary sources and n denotes the sample number. The objective of the system is to minimize $\mathbf{e}(n) = \mathbf{d}(n) + \mathbf{y}(n)$, in which $\mathbf{e}(n) \in \mathcal{R}^{L_{\text{perf}} \times P}$ is the output of the KHI, named the performance signal, and $\mathbf{y}(n) \in \mathcal{R}^{L_{\text{perf}} \times P}$ is the secondary signal which is the output of the KHI due to the secondary sources.

The secondary signal is the control output signal $\mathbf{u}(n) \in \mathcal{R}^{M \times P}$, in which M denotes the number of secondary sources, filtered by the secondary path $\mathbf{G}(z) \in \mathcal{R}^{L_{\text{perf}} \times M}$, following

$$\mathbf{y}(n) = \mathbf{G}(z)\mathbf{u}(n), \tag{5}$$

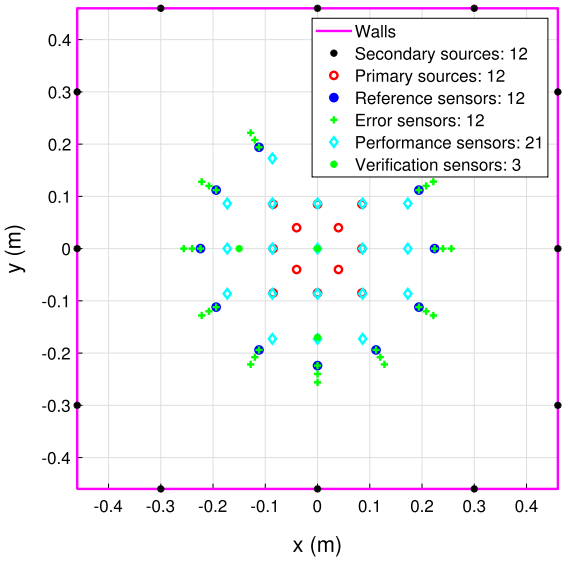

Fig. 5. 2D schematic view of the experimental setup.

in which z denotes the unit-delay forward shift operator. The control output signal $\mathbf{u}(n)$ is the reference signal $\mathbf{x}(n) \in \mathcal{R}^{K \times P}$, in which K denotes the number of reference sensors, filtered by the control coefficients $\mathbf{W}(z) \in \mathcal{R}^{M \times K}$, written as

$$\mathbf{u}(n) = \mathbf{W}(z)\mathbf{x}(n). \tag{6}$$

Assuming that the filters are time-invariant, the filtered-reference signals $\mathbf{r}(n) \in \mathcal{R}^{L_{\text{perf}} \times MK}$ are written as

$$\mathbf{r}(n) = \mathbf{G}(z)\mathbf{x}(n), \tag{7}$$

so that the performance signal can be written as

$$\mathbf{e}(n) = \mathbf{d}(n) + \mathbf{r}(n)\mathbf{W}(z). \tag{8}$$

The cost function is written as the expectation of the sum of the squared performance signals

$$J = \mathrm{E}\left[\mathbf{e}^T(n)\mathbf{e}(n)\right], \tag{9}$$

in which $\mathrm{E}[\cdot]$ denotes the expectation operator and the superscript $(\cdot)^T$ denotes the matrix transpose. The optimal set of control filters is found by taking the derivative of the cost function with respect to the control filters and equating this to zero, following

$$\frac{\partial J}{\partial \mathbf{W}(z)} = 2\mathrm{E}\left[\mathbf{r}^T(n)\mathbf{r}(n)\right]\mathbf{W}(z) + 2E\left[\mathbf{r}^T(n)\mathbf{d}(n)\right] = 0. \tag{10}$$

Following [24], an iterative procedure with regularization is assumed to solve for $\mathbf{W}(z)$ in which $\mathbf{W}_k(z)$ is the approximation of $\mathbf{W}(z)$ at iteration k, written as

$$\mathbf{R}_k = \mathbf{b} - \mathbf{T}_B\mathbf{W}_k(z), \tag{11}$$

in which

$$\mathbf{T}_B = \mathrm{E}\left[\mathbf{r}^T(n)\mathbf{r}(n)\right] + \beta\mathbf{I}, \tag{12}$$

$$\mathbf{b} = \mathrm{E}\left[\mathbf{r}^T(n)\mathbf{d}(n)\right], \tag{13}$$

in which β is the optional regularization parameter and $\mathbf{R}_k$ is the residual at iteration k. The matrix has a Toeplitz-block structure in the case of a system with multiple secondary sources M and multiple reference sensors K. This matrix is structured as

$$\mathbf{T}_B = \begin{bmatrix} \mathbf{T}_{11} & \mathbf{T}_{12} & \cdots & \mathbf{T}_{1N} \\ \mathbf{T}_{21} & \ddots & & \vdots \\ \vdots & & & \\ \mathbf{T}_{N1} & \cdots & \cdots & \mathbf{T}_{NN} \end{bmatrix}, \tag{14}$$

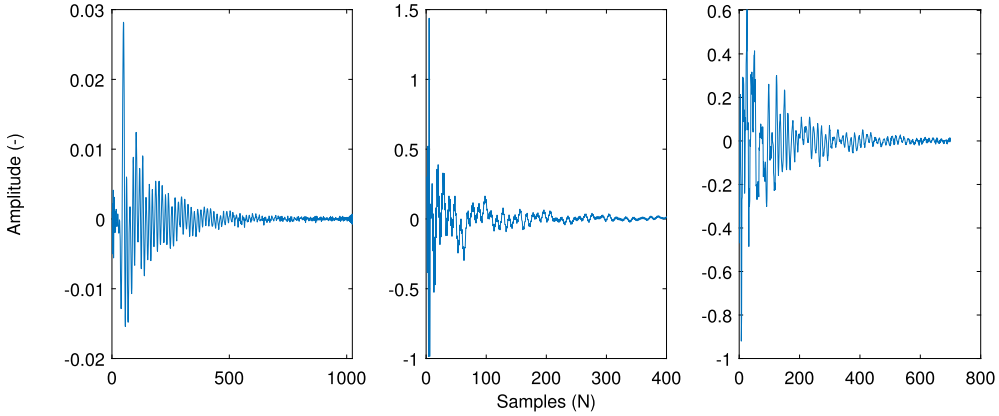

Fig. 6. Impulse responses of the system. The left figure shows the impulse response of the primary path, from the first primary source to the first performance sensor. The middle figure shows the impulse response of the secondary path, from the first secondary source to the first performance sensor. The right figure shows the feedback path, from the first secondary source to the first reference sensor.

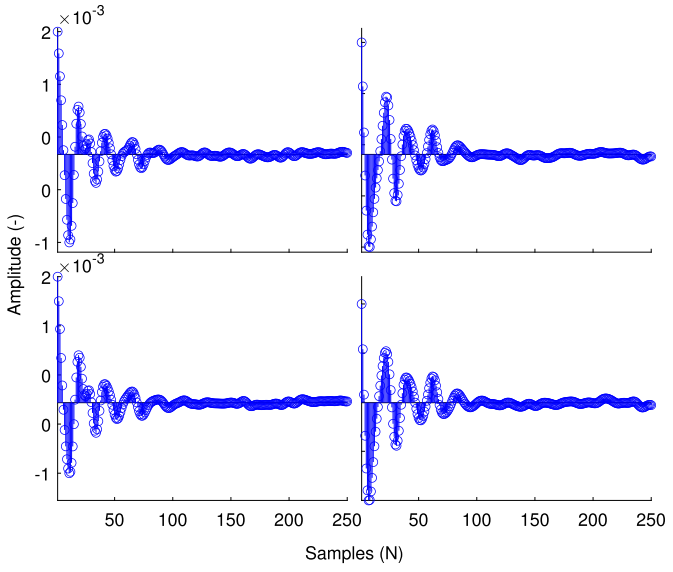

Fig. 7. The control filter coefficients $\mathbf{W}(z)$ of length $I = 250$ samples. The filter coefficients correspond to reference sensors $1, 2$ and secondary sources $1, 2$. The other channels are omitted for the sake of readability.

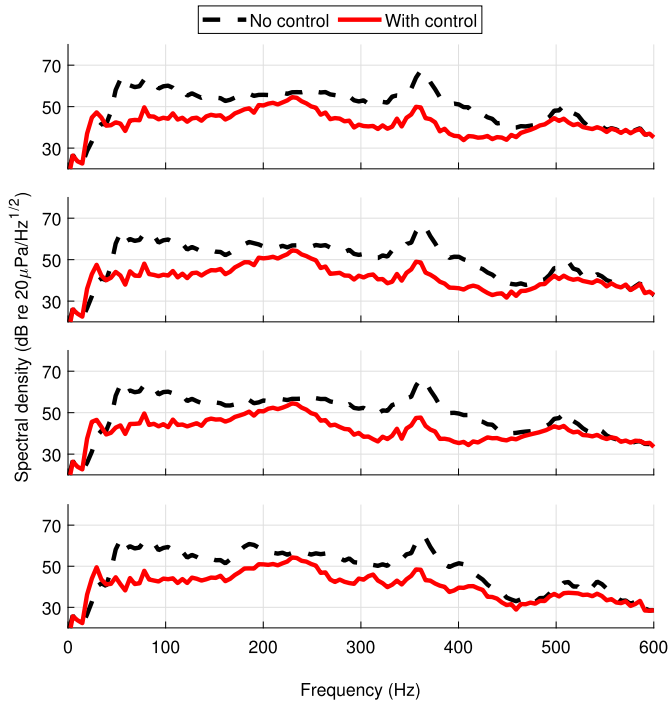

Fig. 8. Spectral densities of the signals at the first four performance sensors. The reduction levels from top to bottom respectively are 8.9, 10.2, 9.7 and 9.7 dB.

in which $N = MK$ and each block $\mathbf{T}_{ij}$ has size I-by-I. Typically, the matrix $\mathbf{T}_B$ is of dimensions MKI-by-MKI. However, each non-symmetric block $\mathbf{T}_{ij}$ is fully defined by the first element of each row and column. Therefore, the matrix $\mathbf{T}_B$ can be stored using $(2I-1)M^2K^2$ elements. The update of the controller matrix $\mathbf{W}_k(z)$ is defined by

$$\mathbf{W}_k(z) = \mathbf{W}_{k-1}(n) + \alpha_k \mathbf{p}_k, \tag{15}$$

in which α_k is a scalar quantity that defines the orthogonal steepest-descent directions [25], which are written as [26]

$$\alpha_k = \frac{\mathbf{R}_{k-1}^T \mathbf{z}_{k-1}}{\mathbf{p}_k^T \mathbf{v}_k}, \tag{16}$$

in which

$$\mathbf{v}_k = \mathbf{T}_B \mathbf{p}_k, \tag{17}$$

which can be computed efficiently. Any Toeplitz matrix $\mathbf{T} \in \mathcal{R}^{n\times n}$ can be embedded into a $2n$-by-$2n$ circulant matrix, following [24]

$$\underbrace{\begin{bmatrix} \mathbf{T} & \times \\ \times & \mathbf{T} \end{bmatrix}}_{\mathbf{C}} \begin{bmatrix} \mathbf{p} \\ \mathbf{0} \end{bmatrix} = \begin{bmatrix} \mathbf{Tp} \\ \dagger \end{bmatrix}, \tag{18}$$

in which $\mathbf{C} \in \mathcal{R}^{2n\times 2n}$ is a circulant matrix, which has the property that it can be diagonalized by the Fourier matrix $\mathcal{F}$, following

$$\mathbf{C} = \mathcal{F}^* \mathbf{\Lambda} \mathcal{F}, \tag{19}$$

in which the superscript $(\cdot)^*$ denotes the conjugate transpose and $\mathbf{\Lambda}$ is the eigenvalue matrix. This technique can also be applied in the Toeplitz-block case. The matrix $\mathbf{T}_B$ is embedded into a block circulant matrix $\mathbf{C}_n \in \mathcal{R}^{2N\times 2N}$, in which each block itself is a $2I$-by-$2I$ circulant matrix. The vector $\mathbf{p}_k$ is extended to a $4IN$-vector by putting zeros in the appropriate places. Then the solution can efficiently be obtained using FFTs [24]. Substitution of Eq. (15) into Eq. (11) and using Eq. (17) leads to

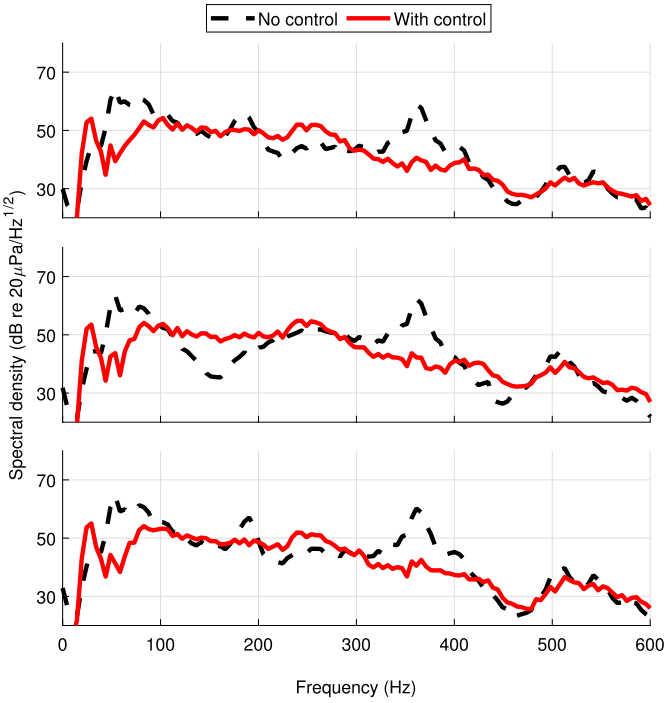

Fig. 9. Spectral density of the signals measured by the verification sensors. The reduction levels from top to bottom respectively are 4.7, 3.6 and 5.0 dB.

$$\mathbf{R}_k = \mathbf{R}_{k-1} - \alpha_k \mathbf{v}_k. \tag{20}$$

The PCG directions are given by [26]

$$\mathbf{p}_k = \begin{cases} \mathbf{z}_{k-1}, & k = 1, \\ \mathbf{z}_{k-1} + \beta_k \mathbf{p}_k, & k > 1, \end{cases} \tag{21}$$

in which

$$\beta_k = \frac{\mathbf{R}_{k-1}^T \mathbf{z}_{k-1}}{\mathbf{R}_{k-2}^T \mathbf{z}_{k-2}}, \tag{22}$$

and $\mathbf{z}_k$ is computed by solving

$$\mathrm{circ}^1(\mathbf{T}_B)\mathbf{z}_k = \mathbf{R}_k, \tag{23}$$

in which $\mathrm{circ}^1(\mathbf{T}_B)$ is the preconditioner, a block circulant approximation to each individual block in the Toeplitz matrix [14]. This preconditioner is computed as the solution to the following optimization problem

$$\min_{\mathbf{C}} \|\mathbf{C} - \mathbf{A}\|_F, \tag{24}$$

in which the subscript $(\cdot)_F$ denotes the Frobenius norm, $\mathbf{C}$ denotes the preconditioning matrix and $\mathbf{A}$ denotes any general matrix. This minimization problem applies to any general matrix $\mathbf{A}$, but in the case of a Toeplitz matrix $\mathbf{T}$, the entries of the preconditioner are given by [14]

$$c_j = \frac{j t_{m-j} + (m-j) t_j}{m}, \quad j = \pm 1, \ldots, \pm(m-1), \tag{25}$$

in which t denotes an entry of the Toeplitz matrix $\mathbf{T}$ and m denotes the size of the Toeplitz matrix. This preconditioning technique is extended to the Toeplitz-block case, in which the preconditioning approach is applied to each individual block in the Toeplitz-block matrix. The preconditioner is computed as the block-circulant approximation to the Toeplitz-block matrix, written as

$$\mathrm{circ}^1(\mathbf{T}_B) = \begin{bmatrix} \mathrm{circ}(\mathbf{T}_{11}) & \mathrm{circ}(\mathbf{T}_{12}) & \ldots & \mathrm{circ}(\mathbf{T}_{1N}) \\ \mathrm{circ}(\mathbf{T}_{21}) & \ddots & & \vdots \\ \vdots & & & \\ \mathrm{circ}(\mathbf{T}_{N1}) & \ldots & \ldots & \mathrm{circ}(\mathbf{T}_{NN}) \end{bmatrix}, \tag{26}$$

in which $\mathrm{circ}(\cdot)$ denotes the circulant preconditioner as defined in Eq. (25). At each iteration of the PCG, Eq. (23) must be solved. Similar to computing Eq. (17), Eq. (23) can be solved efficiently using FFTs. Each block $\mathrm{circ}(\mathbf{T}_{ij})$ is circulant, so that

$$\mathrm{circ}(\mathbf{T}_{ij}) = \mathcal{F}^* \mathbf{\Lambda}_{ij} \mathcal{F}. \tag{27}$$

Let $\tilde{\mathcal{F}} = \mathbf{I} \otimes \mathcal{F}$, a block diagonal matrix with the Fourier matrix $\mathcal{F}$ repeated along the diagonal. Define $\mathbf{P}$ as the permutation matrix that satisfies

$$\left(\mathbf{P}^* \mathbf{T}_{mn} \mathbf{P}\right)_{k,l;i,j} = \left(\mathbf{T}_{mn}\right)_{i,j;k,l}, \tag{28}$$

for $1 \le i, j \le n$, $1 \le k, l \le m$. The dense matrix $\mathbf{D}_m \in \mathcal{R}^{N \times N}$ is defined as

$$\left(\mathbf{D}_m\right)_{ij} = \left(\mathbf{\Lambda}_{ij}\right)_m. \tag{29}$$

Then, Eq. (23) is solved by computing [14]

$$\mathbf{z}_k = \tilde{\mathcal{F}}^* \left\{ \mathbf{P}^T \left[\mathrm{diag}(\mathbf{D}_1^{-1}, \ldots, \mathbf{D}_I^{-1}) \left(\mathbf{P} \left(\tilde{\mathcal{F}} \mathbf{R}_k \right) \right) \right] \right\}. \tag{30}$$

The algorithm is terminated as soon as the maximum number of iterations is reached, or if the relative tolerance is achieved, written as

$$\left| \frac{\mathbf{R}_k^T \mathbf{R}_k}{\mathbf{R}_0^T \mathbf{R}_0} \right| < \epsilon, \tag{31}$$

in which ϵ is the relative tolerance parameter.

4. Real-time active suppression of acoustic reflections in a small-scale anechoic chamber

The experimental setup being used is shown in Fig. 3. The height of the setup is limited to 20 cm, so that the sound field is considered 2D up to about 850 Hz, which is above the frequency range of interest. Both the width and the length are 0.92 m. The setup consists of 12 independent secondary sources (Visaton W130X) placed at the edge. Each side has 3 secondary sources, with a spacing of 0.3 m in which the middle one is centered. The top of the setup is covered by a plate of glass with a thickness of 1.2 cm. The setup is equipped with 12 external independent primary sources (Visaton W130X). Each primary source is placed in a box with outer-dimensions of $(w, l, h) = (0.24, 0.24, 0, 29)$ m, being the width, length and height respectively. Each primary source box is connected to the center of the setup with a tube of length 1 m, as shown in Fig. 4. The locations of the tubes connected to the setup are shown in Fig. 5.

The setup is equipped with a total of 39 KECG2240PBJ condenser microphones. The setup is equipped with $K = 12$ reference sensors, which are located at the coordinates $(x_r, y_r) = (\{r_s - h\}\cos\theta_r, \{r_s - h\}\sin\theta_r)$, in which $r_s = 0.24$ m, $\theta_r = 2\pi i/K$, $i = 0, \ldots, K-1$ and $h = 1.6$ cm. The 36 error microphones are placed at the coordinates $(x_e, y_e) = (\{r_s, r_s \pm h\}\cos\theta_e, \{r_s, r_s \pm h\}\sin\theta_e)$, in which $\theta_e = 2\pi i/L$, $i = 0, \ldots, L-1$, resulting in $L = 12$ error sensors on a circle with each three microphones aligned in radial direction. With all the inner and outer microphones at the circle, the particle velocity is estimated using Eq. (4). With the middle microphones the acoustic pressure is measured. The particle velocity and acoustic pressure at the circle are the input of the KHI, with $\rho = 1.21$ kg/m^3 and $c = 343$ m/s, to compute the primary path $\mathbf{P}(z)$ and the secondary path $\mathbf{G}(z)$ at $L_{\mathrm{perf}} = 21$ performance sensor locations, which are equally distributed within the circle as shown in Fig. 5.

The setup contains 3 verification sensors, at $(x, y) = (-0.15, 0)$ m, $(0, 0)$ m and $(0, -0.17)$ m, for sensor 1 to 3 respectively. The placement of the verification sensors is indicated in Fig. 5. The verification sensors measure the total acoustic pressure and are used to estimate the

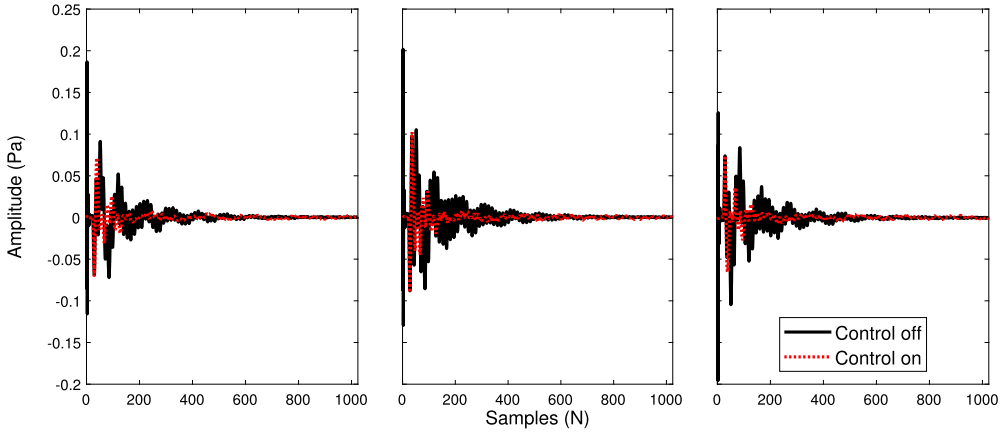

Fig. 10. The impulse response from the primary sources to the verification sensors with the controller turned off and with the controller turned on.

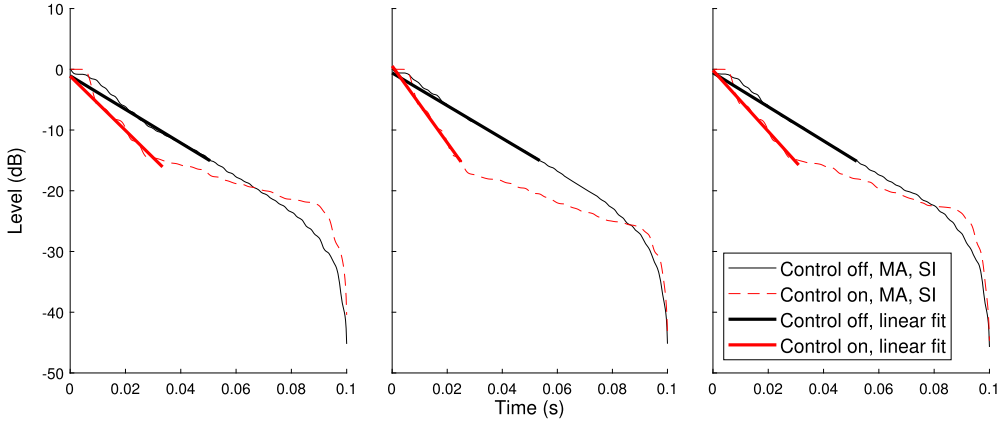

Fig. 11. An estimation of the RT (T10) using a smoothed envelope of the impulse response. The left figure is the first verification sensor; without control the RT is 0.036 s and with control the RT is 0.022 s. The middle figure is the second verification sensor; without control the RT is 0.037 s and with control the RT is 0.016 s. The right figure is the third verification sensor; without control the RT is 0.036 s and with control the RT is 0.020 s.

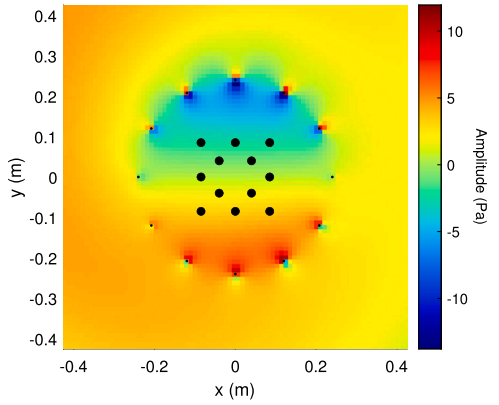

Fig. 12. With the primary sources active, located at the black dots. The result is only valid inside the contour.

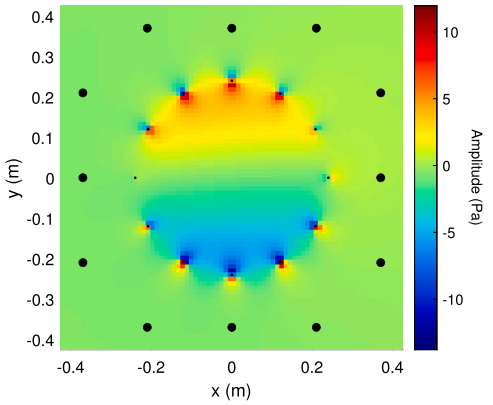

Fig. 13. With the secondary sources active, located at the black dots. The result is only valid inside the contour.

RT. All the physical microphones are individually calibrated using an Acoustical Calibrator Type 4231, at 1000 Hz, 94 dB. The controller is a Speedgoat machine with multiple IO135 modules, interconnected via their digital ports for synchronization. The system runs at a sampling frequency of $f_s = 5$ kHz. The microphones are connected to custom made pre-amplifiers, which are connected to the control machine. The sources are connected to a Dayton Audio MA1240a multizone amplifier, which is connected to the control machine. The reference signals are filtered by a 3rd order high-pass filter having a cutoff frequency at 20 Hz. The error signals and verification signals are filtered by a 3rd order low-pass filter having a cutoff frequency at 600 Hz and a 3rd order high-pass filter with a cutoff frequency at 60 Hz. All individual sources generate a logarithmic sweep from 20 to 600 Hz to identify the system. The impulse responses of the system are shown in Fig. 6. The left figure shows the primary path, from the primary sources to the error sensors, truncated to $P = 1024$ samples. The middle figure shows the secondary path, from the secondary sources to the error sensors, truncated to $J = 400$ samples. The right figure shows the feedback

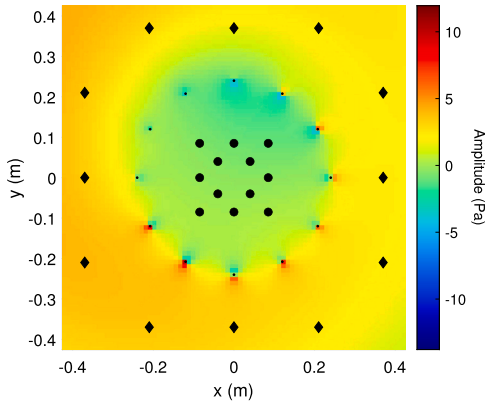

Fig. 14. Sum of Figs. 12 and 13.

path, from the secondary sources to the reference sensors, truncated to $F = 700$ samples. The feedback path is used to apply IMC.

A set of control filter coefficients $\mathbf{W}(z)$ is computed, which minimize the signals of the performance sensors. The control filter coefficients of length $I = 250$ samples are obtained after running the PCG algorithm, using a relative tolerance of $\epsilon = 1 \times 10^{-6}$, with the regularization parameter $\beta = 1 \times 10^{-1}$. By setting the regularization parameter at this value, a stable system is maintained in combination with IMC. The algorithm required 102.5 s on a desktop computer with an Intel core i7 − 8700 @ 3.20 GHz CPU and 64 GB of RAM. The filter coefficients are shown in Fig. 7.

During real-time control, each primary source generates an independent logarithmic sweep from 20 to 600 Hz, which is randomly varied in duration and starting time for each primary source.

The spectral density of the first four performance signals measured at the performance sensor locations is shown in Fig. 8. This shows that the controller reduces the signals as computed by the KHI up to about 600 Hz by an average of 9.6 dB. The spectral density of the signals measured by the verification sensors is shown in Fig. 9, with an average reduction of 4.4 dB. From this figure can be seen that the spectral density becomes increasingly flat. The impulse response from the primary sources to the verification sensors with- and without control is shown in Fig. 10. The figures show that the amplitude of the impulse response is reduced with the controller turned on, although the active control system increases the noise floor as can be seen when the impulse response has decayed.

The RT is estimated using the envelope of the impulse response, after which a moving average filter is applied using a window of 10 samples, followed by the Schroeder integration method [27], using a time limit of 500 samples. A first order fit is made from −5 dB to −15 dB, resulting in an estimation of T10, as shown in Fig. 11. The slope (A) of this fit is used to estimate the RT following

$$RT = \frac{-60}{A}. \tag{32}$$

The RT has been reduced from 0.036 s to 0.022 s, 0.037 s to 0.016 s and 0.036 s to 0.020 s at verification sensors 1 to 3 respectively. The result of the KHI at $f = 215$ Hz is shown in Fig. 12 with the primary sources active, Fig. 13 with the secondary sources active and the sum of both in Fig. 14. From the sum of both fields can be seen that global control of the area within the circle of microphones is achieved. It should be noted that the results of the KHI are not valid outside the contour, but the full domain is shown for completeness.

5. Conclusion

A formulation of the modified preconditioned conjugate gradient time-domain algorithm for a fixed-gain active noise control system is presented. The algorithm applies block-circulant preconditioning to improve convergence speed. The algorithm is used to compute a set of control filters for the real-time suppression of reflections from the walls of a small-scale 2-dimensional setup. The reflected sound field is computed with the Kirchhoff-Helmholtz integral, using microphone triplets placed on a circle within the setup. The real-time control manages to reduce the average of the performance signals by 9.6 dB. The setup is equipped with verification sensors, at which an average reduction of 4.4 dB is achieved, and the spectral density has become increasingly flat. The verification sensors are used to estimate the reverberation time, which has been reduced by using the active control system.

CRediT authorship contribution statement

R. Haasjes: Writing – review & editing, Writing – original draft, Visualization, Software, Project administration, Methodology, Investigation, Formal analysis, Data curation, Conceptualization. **A.P. Berkhoff:** Writing – review & editing, Supervision, Software, Project administration, Methodology, Funding acquisition.

Declaration of competing interest

The authors declare that they have no known competing financial interests or personal relationships that could have appeared to influence the work reported in this paper.

Data availability

The authors are unable or have chosen not to specify which data has been used.

Acknowledgements

This research is funded by TNO. The support and funding from TNO are gratefully acknowledged. The authors would like to thank Henny Kuipers for the design of the custom pre-amplifier hardware and Axel Lok for the help with facilitating and assembling the experimental setup and calibration of the microphones. The authors would like to thank the reviewers for taking the time and effort to review the manuscript. The comments and suggestions are sincerely appreciated and helped to improve the quality of the manuscript.

References

[1] Kopiev VF, Palchikovskiy VV, Belyaev IV, Bersenev YV, Makashov SY, Khramtsov IV, et al. Construction of an anechoic chamber for aeroacoustic experiments and examination of its acoustic parameters. Acoust Phys 2017;63(1):113–24.
[2] Patchett BD, Anderson BE. Nonlinear characteristics of high amplitude focusing using time reversal in a reverberation chamber. J Acoust Soc Am 2022;151(6):3603–14.
[3] Sozanski K, Sozanska A. Low frequency loudspeaker measurements using an anechoic acoustic chamber. In: 2018 signal processing: algorithms, architectures, arrangements, and applications (SPA); 2018. p. 367–72.
[4] Schneider S, Kern C. Acoustical behavior of the large anechoic chamber at the laboratoire de Mécanique et d'Acoustique in the low frequency range. Acta Acust Acust 2008;94:141–7.
[5] Belyaev IV, Golubev AY, Zverev AY, Makashov SY, Palchikovskiy VV, Sobolev AF, et al. Experimental investigation of sound absorption of acoustic wedges for anechoic chambers. Acoust Phys 2015;61(5):606–14.
[6] Cuyx B, Desmet W, Buyens W, van Waterschoot T. Design and validation of a low-cost acoustic anechoic chamber. J Audio Eng Soc 2020;149:1–5.
[7] Ressl MS, Wundes PE. Design of an acoustic anechoic chamber for application in hearing aid research. In: Proceedings of the 11th WSEAS international conference on acoustics & music: theory & applications. Iasi, Romania: World Scientific and Engineering Academy and Society (WSEAS); 2010. p. 18–23.
[8] Duanqi X, Zheng W, Jinjing C. Acoustic design of an anechoic chamber. Appl Acoust 1990;29(2):139–49.
[9] Lu L, Yin K, de Lamare RC, Zheng Z, Yu Y, Yang X, et al. A survey on active noise control in the past decade—part i: linear systems. Signal Process 2021;183:108039.
[10] Elliott SJ. Signal processing for active control, signal processing and its applications. California, USA: Academic Press; 2001.

[11] Friot E, Guillermin R, Winninger M. Active control of scattered acoustic radiation: a real-time implementation for a three-dimensional object. Acta Acust Acust 2006;92:278–88.
[12] Friot E, Bordier C. Real-time active suppression of scattered acoustic radiation. J Sound Vib 2004;278(3):563–80.
[13] Levinson N. The Wiener (root mean square) error criterion in filter design and prediction. J Math Phys 1946;25(1–4):261–78.
[14] Chan TF, Olkin JA. Circulant preconditioners for Toeplitz-block matrices. Numer Algorithms 1992;6:89–101.
[15] Cai M, Jin X, Wei Y. A generalization of T. Chan's preconditioner. Linear Algebra Appl 2005;407:11–8.
[16] Lv X, Huang T, Ren Z. A modified T. Chan's preconditioner for Toeplitz systems. Comput Math Appl 2009;58(4):693–9.
[17] Becker TS, Van Manen D-J, Donahue CM, Bärlocher C, Börsing N, Broggini F, et al. Immersive wave propagation experimentation: physical implementation and one-dimensional acoustic results. Phys Rev X 2018;8(3).
[18] Börsing N, Becker TS, Curtis A, van Manen D-J, Haag T, Robertsson JO. Cloaking and holography experiments using immersive boundary conditions. Phys Rev Appl 2019;12:024011.
[19] Thomsen HR, Molerón M, Haag T, van Manen D-J, Robertsson JOA. Elastic immersive wave experimentation: theory and physical implementation. Phys Rev Res 2019;1:033203.
[20] Li X, Robertsson J, van Manen D-J. Elastic immersive wave experimentation. Geophys J Int 2022;233(1):724–39.
[21] Habault D, Friot E, Herzog P, Pinhede C. Active control in an anechoic room: theory and first simulations. Acta Acust Acust 2017;103:369–78.
[22] Haasjes R, Berkhoff AP. An efficient offline scheme to compute an FIR controller for active reduction of acoustic reflections in an anechoic chamber. J Sound Vib 2024;573:118198.
[23] Hulsebos E, de Vries D, Bourdillat E. Improved microphone array configurations for auralization of sound fields by wave-field synthesis. J Audio Eng Soc 2002;50(10):779–90.
[24] Chan RH-F, Jin X-Q. An introduction to iterative Toeplitz solvers. Society for Industrial and Applied Mathematics; 2007.
[25] Berkhoff AP, Thijssen JM, van den Berg PM. Ultrasound wave propagation through rough interfaces: iterative methods. J Acoust Soc Am 1996;99:1306–14.
[26] Golub GH, Van Loan CF. Matrix computations. Johns Hopkins University Press; 1989.
[27] Schroeder MR. New method of measuring reverberation time. J Acoust Soc Am 1965;37(3):409–12.